Gabrielse Christine (Orcid ID: 0000-0001-6905-2288)
Pinto Victor, A. (Orcid ID: 0000-0003-1210-167X)
Nishimura Yukitoshi, Toshi (Orcid ID: 0000-0003-3126-4394)
Lyons Larry, R. (Orcid ID: 0000-0002-9867-3638)
Gallardo-Lacourt Bea (Orcid ID: 0000-0003-3690-7547)
Deng Yue (Orcid ID: 0000-0002-8508-1588)

Storm-time meso-scale plasma flows in the nightside high-latitude ionosphere: A statistical survey of characteristics

Christine Gabrielse[1,2], Victor Pinto[1], Yukitoshi Nishimura[1,3], Larry Lyons[1],
Bea Gallardo-Lacourt[4], Yue Deng[5]

1. Department of Atmospheric and Oceanic Sciences, University of California, Los Angeles, CA
2. Earth, Planetary, and Space Sciences Department, University of California, Los Angeles, CA
3. Boston University, Boston, MA
4. University of Calgary, Alberta
5. University of Texas, Arlington, TX

Corresponding author: Christine Gabrielse ● cgabrielse@ucla.edu

Key Points:

1. Auroral oval mesoscale flow width PDFs are similar for CMEs & HSSs, but in the polar cap wider flows are more probable during CMEs.

2. More fast meso-scale flows >400 m/s occur during CMEs than during HSS storms, which have very few >400 m/s flows.

3. Faster flows occur during storm main phase, more flows occur during recovery phase—which has a similar occurrence rate to non-storm time.

Abstract

Although much work has been done to characterize the global response of Earth's upper atmosphere to geomagnetic storms, much is unknown regarding the response on meso-scales (~30-500 km). In order to understand how the nightside, high-latitude ionosphere responds on these scales during storms, we have characterized widths, velocities, and occurrence rates of equatorward and poleward meso-scale flows. We characterized them according to main phase vs. recovery phase as well as coronal mass ejection (CME) vs. high-speed stream (HSS) storms. Some results include the following: Mesoscale flows are faster during the main phase of the storms. Faster flows >400 m/s are more frequent and probable during CME storms as compared to HSS storms, but more flows occur during HSS storms. Polar cap flows are wider during CMEs than during HSSs. There is a post-midnight preference for polar cap meso-scale flows during storms, especially during recovery phase and during HSSs.

Plain Language Summary

Geomagnetic storms are the Sun's most effective way to transport energy from the solar wind into the Earth system. The type of storm and the phase of the storm (its developing vs. its recovering) drives Earth's system differently, and therefore creates different types of disturbances to Earth's nearby space and upper atmosphere. Our study characterizes and contrasts one type of disturbance—30-500 km wide, nightside upper atmosphere plasma flows—during two types of storms and during the two storm phases. We found the flow characteristics are different between the types and phases of storms. For example, more flows occur during one type of storm, but faster flows occur during the other. These plasma flows have not been studied until recently, but their effects may be very important to the global Earth system. Our results can be input into global models to improve them and to better understand and predict Earth's response to storms.

1. Introduction

Knowing how the Earth's upper atmosphere reacts to different inputs from the solar wind is important in understanding how the magnetosphere-ionosphere-thermosphere system is coupled. These reactions help elucidate space weather phenomena as well as help improve models and predictive capabilities which, in turn, help protect spaceborne assets. Both ground (e.g., Cousins and Shepherd, 2010) and spacecraft (e.g., Haaland et al., 2007) observations have been utilized to create empirical models of the global convection pattern under different interplanetary magnetic field (IMF) conditions. These global responses, and how they affect heating of the upper atmosphere in a global sense, are well-modeled and understood (e.g., Roble and Ridley, 1994; Fuller-Rowell et al., 1996; Weimer, 1996; Ridley et al., 1998; 2000; 2006). The global response, however, has proved inadequate to explain the total heating observed. Global models tend to underestimate (or miss altogether) contributions from smaller-scale structures (e.g. Codrescu et al. 1995; Deng and Ridley, 2007; Matsuo et al. 2003), which provide a large amount of energy to the coupled magnetosphere-ionosphere-thermosphere system (Angelopoulos et al., 1994). This was in part due to the low resolution of Global Climate Models; however, modern models such as the Global Ionosphere–Thermosphere Model (GITM) (Ridley et al., 2006) have recently achieved appropriate resolution (e.g., Guo et al. 2018) and now require data to inform them.

The dynamic phenomena occurring on smaller, meso-scales (30-500 km) may contribute significantly to the total heating and therefore are important to characterize (Codrescu et al., 1995). As this fact became more apparent, studies were designed to better understand meso-scale phenomena (e.g., Kivanç and Heelis, 1998; Johnson and Heelis, 2005; Rinne et al., 2007; Moen et al., 2008; Oksavik et al., 2011; Cousins and Shepherd, 2012; McGranaghan et al., 2017; Gabrielse et al., 2018; Chen et al., 2018]; yet much remains to be characterized to adequately integrate these meso-scales into global models. More specifically,

fast meso-scale flows in the ionosphere may contribute to intense thermosphere heating and upwelling, which can increase thermospheric densities and thus drag on low-altitude satellites (Storz et al., 2005; Knipp et al., 2013).

Ground-based radars, such as Super Dual Auroral Radar Network (SuperDARN) HF radars (Greenwald et al., 1995) and the European Incoherent Scatter (EISCAT) radars, are useful tools to study meso-scale ionosphere flows given their ability to measure flow properties in two dimensions at the same location continuously. Sunward flows, or "reversed flow events", have been reported in the polar cusp by EISCAT as potential signatures of dayside reconnection events, and are related to distinct auroral arcs (Rinne et al., 2007; Moen et al., 2008; Oksavik et al., 2011). Both anti-sunward (equatorward on the nightside) and sunward (poleward on the nightside) high-latitude flows have been observed by EISCAT (Pitkänen et al., 2011) and SuperDARN (Gallardo-Lacourt et al., 2014), and were correlated with equatorward-propagating auroral streamers observed by conjugate Kevo all-sky cameras (Syrjäsuo, 2001) and THEMIS auroral all-sky-imagers (Mende et al., 2008). Using 135 events, Gallardo-Lacourt et al. (2014) found that the equatorward flows had an average width of ~75 km and occurred predominantly in the pre-midnight sector, whereas poleward flows had an average width of ~76 km and occurred predominantly in the post-midnight sector.

Gabrielse et al. (2018) extended their work by building a database of polar cap and auroral oval equatorward and poleward flows observed by the poleward-facing SuperDARN stations at Rankin Inlet and Saskatoon throughout 2008-2016. Collecting flow data within two hours of midnight—to capture flows that were predominantly anti-sunward or sunward—they determined meso-scale flow characteristics under different substorm and solar cycle activity levels, different IMF clock angles, and different latitudes. They found meso-scale polar cap flow speeds increased under a more active part of the solar cycle (measured by F10.7), whereas the auroral oval meso-scale flow speeds remained similar across the solar

cycle. They found that the flow width was consistent across various AL indices and between summer and winter seasons (~180 km in the polar cap and 140-150 km in the auroral oval); however, the polar cap meso-scale flow width did increase slightly during the more active part of the solar cycle. Although fairly comprehensive, Gabrielse et al. (2018) did not examine how storms affect meso-scale flow characteristics. Geomagnetic storms are periods of extremely efficient energy transfer from the solar wind to Earth's magnetosphere and are especially dangerous periods for Earth-orbiting satellites (Gonzalez et al., 1989; 1994). Therefore, this paper characterizes meso-scale flows in the high-latitude ionosphere by studying how their attributes shift under different storm-time conditions. Specifically, we studied flow occurrence rates, flow widths, and flow velocities during different phases of the magnetic storm (main phase vs. recovery phase) and storm type (coronal mass ejection vs. high speed stream).

Coronal mass ejections (CMEs) occur when a massive amount of material is ejected from the sun's surface. They are led by a sheath of compressed solar wind, which is typically led by a shock. CMEs occur more frequently during solar maximum (Webb, 1991; Yashiro et al., 2004). High speed streams (HSSs) emanate from a coronal hole and are generally not led by a shock when they impact the Earth. They occur more frequently during the late declining stage of the solar cycle (Mursula and Zeiger, 1996). The interplanetary magnetic field (IMF) within a HSS is highly variable, so HSS storms tend to be less geoeffective than CMEs—though HSSs typically last longer. Because CME and HSS storms have different drivers (Gonzalez et al., 1999), the magnetosphere responds differently in at least 21 different ways (Borovsky and Denton, 2006; Denton et al., 2006; Cramer et al., 2013; Chen et al., 2014; Shen et al. 2017). It is therefore expected that meso-scale ionosphere flows will differ under different storm types, and this paper quantifies those differences.

2. Methodology

In this study, we utilized the database of meso-scale flows collected by Gabrielse et al. (2018) spanning from 2008-2016 from Rankin Inlet (62.82⁰ N, -93.11⁰ E in geographic; 72.6⁰ N, -26.4⁰ E in magnetic), updated to include some missing dates. The database provides the flow width, speed, and location, which was converted into magnetic local time (MLT). The flows and their characteristics were determined for each radar scan, which occur with a 1-2 min cadence. Therefore, throughout this study, when we refer to a flow we are referring to meso-scale flow characteristics measured during a single radar scan. Gabrielse et al. (2018) separated the flows into the polar cap or the auroral oval automatically using a median filter algorithm of spectral width values to determine the polar cap boundary location. This method was developed by Chisham et al. (2003; 2004) and Sotirelis et al. (2005), who reported an error of 1-2 range gates (~1⁰ latitude). Gabrielse et al. (2018) validated the algorithm with the aurora from the THEMIS all-sky-imagers when available, finding up to ~2⁰ difference from the auroral PCB. The error is mitigated by the fact that they required at least four range gates meeting their criteria to fall equatorward of the SWB to be considered an auroral flow, and at least four range gates meeting their criteria to fall poleward of the SWB to be considered a polar cap flow.

Regarding the data quality, Reimer et al. (2018) showed that SuperDARN fitted data are good quality for the majority of the time. They noted that in low signal-to-noise ratio and/or low signal-to-clutter regimes, the ad hoc variance and empirical criterion can result in underestimated errors for the fitted parameter because the relative contributions of signal, clutter, and noise to the ACF variance are not considered. We note that Cousins et al. (2013). utilizing an improved SuperDARN assimilative mapping procedure, determined that the dynamic range of the strength of convection is larger than what is reported by the standard

linear regression-based approach. This suggests that our non-storm time flows may be slower, and our storm-time flows may be faster, than what is reported.

To compare the flow characteristics within different storm phases and types, we collected a database of storms also spanning 2008-2016. To find storms automatically, we first searched for all times that SYM-H dipped below -50 nT. Next, we searched within 24 hours for the lowest SYM-H value. We define this SYM-H minimum as the end of the main phase and the beginning of the recovery phase. Because the level of driving is stronger during the main phase, we expected to see differences in meso-scale flow characteristics between the two phases. We defined the main phase start when SYM-H was most positive within 24 hours prior to the SYM-H minimum. We defined the recovery phase end when SYM-H recovered to 80% of its minimum. These were the criteria set by Moya et al. (2017). We categorized each storm as due to a CME, HSS, both (CME+HSS), or other, if the cause was not clear. In addition to Moya et al. (2017), we validated our automatically collected list by comparing with several other storm databases: the Varsiti HSS catalog, the Richardson/Cane CME list, and the Database Of Notifications, Knowledge, Information (DONKI). When we studied flow characteristics binned by CME or HSS, we only used the cases when the storm was clearly a CME or clearly a HSS. The number of flows analyzed per storm type are listed in Table 1. The storm times and classifications, as well as a figure that plots the number of storms per year, are included in the Supplementary Material.

3. Results

3.1 Flow width and speed

We compared the meso-scale flow width and speed between non-storm time, the main phase, and the recovery phase of the storms. Similar to Gabrielse et al. (2018), we plotted

log-normal probability distribution functions (PDFs) for each bin of data in Figure 1, and included the σ and μ values in Table 1.

$$PDF = \frac{log_{10}(e)}{V\sigma\sqrt{2\pi}} exp\left\{-\left[\frac{(log_{10}(V)-\mu)^2}{2\sigma^2}\right]\right\} \tag{1}$$

where V = Velocity (or width, for the width PDFs), μ = mean of $log_{10}(V)$, and σ = standard deviation of $log_{10}(V)$. We also included the number of scans that comprise each of the probability distribution functions presented in our figures in Table 1. We did this for equatorward flows in the polar cap and auroral oval, but only for poleward flows in the polar cap because the statistics were poor (we had too few events) for auroral oval poleward flows. Table 1 displays the median and standard deviation of the flow velocities and widths.

We also performed the Kolmogorov-Smirnov Two Sample test between each distribution that we compared, and listed the results in Table 2. A "unique" result means that the null hypothesis (the two distributions are the same) was rejected; an "indistinct" result means that the two distributions were not significantly different. We reported the 0.05 significance level result, but italicized the text if the 0.10 significance level rejected the null hypothesis. For example, the equatorward flow velocity distributions are indistinct when comparing HSSs and non-storm time flows at the 0.05 significance level; however, they are significantly different if we relax the significance level to 0.10. The details of the test and the results for the 0.10, 0.05, and 0.01 significance levels are included in the Supplementary Material.

We first compared different storm phases with non-storm time statistics. In the polar cap, it is more probable for both equatorward and poleward meso-scale flows to be wider during a storm, especially during the main phase of a storm (except, the poleward flow widths are not significantly different between the recovery phase and non-storm time). In the auroral oval, the flow widths are not significantly different. The most probable speed in the polar cap is fairly constant across storm phases. However, faster flows are more likely during

the main phase than during non-storm or recovery phases, and they are more likely during non-storm time than during the recovery phase. In the auroral oval, faster flows are more likely during storm time, particularly during the main phase.

We next compared width and velocity PDFs between CME and HSS storms. Polar cap flows during CMEs are wider than during non-storm time and during HSSs. The auroral oval flow width PDFs are indistinct. In the polar cap, faster flows (>400 m/s for equatorward flows, ~>325 for poleward flows) are more likely during CMEs, but are less likely during HSSs than during non-storm time. We note that for the 0.05 significance level, the HSS and non-storm time flow distributions are indistinct, but they are significantly different at the 0.10 level. Faster flows are also more likely during CMEs in the auroral oval.

The greater probability for faster flows during CMEs can explain the results from Gabrielse et al. (2018), who reported faster flows in the polar cap during large F10.7 (the solar maximum). The CME occurrence rate strongly peaks during solar maximum (Webb, 1991; Yashiro et al., 2004; see Supplemental Material Figure S1), so storms during solar maximum are more often CME-driven storms (Richardson et al., 2001). For the same reason, the fact that we found wider flows in the polar cap during CMEs also explains why Gabrielse et al. (2018) found wider flows in the polar cap during large F10.7—the only parameter they checked that had any effect on flow width.

3.2 Occurrence Rates

Next, we considered meso-scale flow occurrence rates per MLT bin. The occurrence rates were calculated as the number of scans that observed a meso-scale flow during a particular phase or type of storm, divided by the total number of scans that could have observed a meso-scale flow during that particular phase or type of storm. In counting statistics, the error bar is $\pm\sqrt{standard\ deviation}$. We did this for both equatorward (Figure

2a,b) and poleward flows (Figure 2c,d). We also checked the occurrence rates for flows exceeding 400m/s to compare with Gabrielse et al. (2018), and because of the clear crossover at 400 m/s in the polar cap equatorward flow PDFs.

There is little change between the HSS and CME storm occurrence rates when all flow velocities are considered; however, there are noticeably more >400 m/s flows during CMEs compared to HSSs. Gabrielse et al. (2018) showed that when all flow velocities >100 m/s are considered, ~13-14 equatorward meso-scale flows occur per hour in the polar cap in each MLT bin. Figure 2 shows that the occurrence rates are a little lower in the pre-midnight sector during storm time, but are roughly the same in the post-midnight sector during recovery phase, HSS, and CME storms (~10-13 flows per hour).

The auroral oval flow occurrence rates had larger error bars due to the smaller number of radar scans that occurred within the auroral oval. Meso-scale flows prefer midnight during the main phase, but have no MLT preference in the recovery phase. They do not have an MLT preference during HSS or CME storms. Like the polar cap, there are more >400 m/s flows during CME storms than HSS storms. Excluding the main phase flows, storm-time flows have similar, though more varied, occurrence rates (~11-24 equatorward flows per hour) as all flows (18-20 equatorward flows per hour across MLT bins (Gabrielse et al. 2018)). There are, however, fewer poleward flows during storm time.

There are more storm-time auroral oval flows than polar cap flows per hour, which is what Gabrielse et al. (2018) and Chen et al. (2018) found for meso-scale flows in general. As Gabrielse et al. (2018) pointed out, this is likely due to the numerous plasma sheet flows that form from tail reconnection and map to the auroral oval. Unlike the storm-time polar cap flows—which had a similar MLT dependence as the >400 m/s flows in Gabrielse et al.

(2018)—the storm-time auroral oval flows did not have the same pre-midnight preference as the >400 m/s flows reported in Gabrielse et al. (2018).

Unlike Gabrielse et al. (2018) who showed a symmetric distribution around midnight when all flows were considered, Figure 2 shows that there is a post-midnight preference during storms, especially HSSs and during the recovery phase. To test what may cause the occurrence rate asymmetry seen in the polar cap during storms, we checked the flow speed, IMF B_Y, and AL index, all parameters that Gabrielse et al. (2018) showed affected the polar cap meso-scale flow occurrence rate distribution.

First, Gabrielse et al. (2018) showed that flow speed affects the occurrence symmetry. When only >400 m/s flows were considered, the flows had a post-midnight preference (except for the more active AL bin). However, the hypothesis that storms have faster flows and therefore the flows have a post-midnight preference was rejected. Constraining the storm-time flows to those >400 m/s, we found the same occurrence rates during CMEs (~2-5 equatorward flows per hour and <1 to 1 poleward flows per hour) as Gabrielse et al. (2018) did for all flows >400 m/s. During HSSs, however, the occurrence rates are practically zero for both equatorward and poleward meso-scale flows >400 m/s in the polar cap. The slower flows during HSSs also have a post-midnight preference. In fact, the prevalence for post-midnight flows during HSSs is even stronger than that for CMEs.

Next, Gabrielse et al (2018) showed that + IMF B_Y and small magnitude IMF B_Y (Bz dominating) resulted in a post-midnight preference for >400 m/s flows, whereas – B_Y resulted in a symmetric distribution about midnight. (They defined –B_Y and +B_Y as >0.5 nT and required 5° < |arctan(B_Y/B_Z)| < 90° .) We tested the hypothesis that more storm-time flows occur during + IMF B_Y, but the hypothesis was rejected because significantly more equatorward flows during all storm categories occurred during – IMF B_Y. The significance

test performed is in the Supplementary Materials. The reason we observed more flows during – IMF B_Y appears to be because during both CMEs and HSSs, IMF B_Y was negative ~70% of the time.

Lastly, Gabrielse et al. (2018) showed that during quiet time (AL>-100 nT), >400 m/s polar cap flows occur predominantly in the post-midnight sector; however, during more active time (-100>AL>-300 nT), their distribution is more symmetric about midnight. We therefore tested the hypothesis that there are more storm-time flows during the quiet AL bin vs. the more active AL bin. This hypothesis proved true, with significantly more polar cap flows occurring during the AL>-100 nT bin. The significance test is included in the Supplemental Materials. The prevalence of flows during quiet AL suggests AL is indicative of the post-midnight asymmetry in the polar cap.

We performed the same comparisons and significance tests for the two AL bins during main phase (which did not see a strong post-midnight preference) and recovery phase (which did see a strong post-midnight preference). For the recovery phase, once again the percentage of flows during quiet time is significantly larger than those during the more active AL bin. For the main phase, there is not a significant difference between the percentage of flows observed in the two AL bins. These results are both expected if quiet AL is indicative of post-midnight preference in the polar cap. The significance test is included in the Supplementary Materials.

In summary, the post-midnight preference is stronger during the storm phase and storm type that are also described by quieter AL indices. The AL-dependence for the polar cap flows' post-midnight preference found in Gabrielse et al. [2018] could therefore be the controlling factor in the post-midnight preference found in this study. This post-midnight preference is like that of polar cap arcs (Hosokawa et al., 2010), which predominantly occur on the dawnside (or, post-midnight). Previous studies showed that polar cap arcs occur more frequently during quiet time than active time (Davis, 1963; Lassen, 1972; Ismail et al., 1977). Because the solar wind driving is dying down during recovery phase, it is possible that the recovery phase polar cap arcs and meso-scale flows act more similarly to the arcs and flows during the quiet time than those during the main phase. A more rigorous comparison of polar cap arcs—the auroral manifestation related to polar cap flows--during main phase vs. recovery phase vs. quiet time could be done to validate this postulation.

4. Summary

In summary, we have characterized storm-time, nightside, high-latitude meso-scale ionospheric plasma flows by their widths, flow speed, and occurrence rates. We compared and contrasted storm-time flows that occurred during the main phase vs. the recovery phase of geomagnetic storms and flows that occurred during CMEs vs. HSSs. We found that:

1. Faster equatorward flows are more probable during the storm's main phase.

2. Faster flows are more probable during CMEs, with 400m/s for equatorward (325 m/s for poleward) appearing as a cutoff. Because CMEs occur more frequently during solar max, this can explain why Gabrielse et al. (2018) observed faster flows in the polar cap during large F10.7.

3. More meso-scale flows occur during the recovery phase than during the main phase in the polar cap. Trends also suggest more meso-scale flows occur in the recovery phase than during the main phase in the auroral oval, though more occur at midnight during the main phase. (The preference for midnight flows in the auroral oval during main phase is strong.)

4. The meso-scale flow occurrence rates during the recovery phase is similar to non-storm time occurrence rates, but the occurrence rates during the main phase are smaller.

5. Storm-time polar cap flows of all speeds have a post-midnight preference. This contrasts with the results of *Gabrielse et al.* [2018] who only found fast (>400 m/s) flows to have this post-midnight preference. This preference is more apparent during the recovery phase than during the main phase, and during HSSs than during CMEs.

6. Quiet AL index (AL>-100 nT) appears to be indicative of the post-midnight preference.

7. Storm-time meso-scale flows have a higher occurrence rate in the auroral oval than in the polar cap (similar to meso-scale flows in general).

8. Polar cap flows are wider during the main phase.

9. Polar cap flows are wider during CMEs than during HSSs.

10. Auroral oval flow width is similar during CMEs, HSSs, and non-storm time. (The width probability distributions are indistinct.)

In addition to these qualitative results, we have presented probability distribution functions and their parameters of the meso-scale flow width and velocity under these different circumstances, as well as their numerical occurrence rates. These quantitative results can be used as inputs to global models, such as the Global Ionosphere–Thermosphere Model (GITM) (Ridley et al., 2006), to better model and predict the storm-time response of the night-side upper atmosphere.

References

Angelopoulos, V., C. F. Kennel, F. V. Coroniti, R. Pellat, M. G. Kivelson, R. J. Walker, C. T. Russell, W. Baumjohann, W. C. Feldman, and J. T. Gosling (1994), Statistical characteristics of bursty bulk flow events, J. Geophys. Res., 99(A11), 21257–21280, doi: 10.1029/94JA01263.

Angelopoulos, V., Cruce, P., Drozdov, A. et al. Space Sci Rev (2019) 215: 9. https://doi.org/10.1007/s11214-018-0576-4.

Borovsky, J. E., and M. H. Denton (2006), Differences between CME-driven storms and CIR-driven storms, J. Geophys. Res., 111, A07S08, doi:10.1029/2005JA011447.

Chen, G.-M., J. Xu, W. Wang, and A. G. Burns (2014), A comparison of the effects of CIR- and CME-induced geomagnetic activity on thermospheric densities and spacecraft orbits: Statistical studies, J. Geophys. Res. SpacePhysics,119, 7928–7939, doi:10.1002/2014JA019831.

Chen, Y.-J., & Heelis, R. A. (2018). Mesoscale plasma convection perturbations in the high-latitude ionosphere. Journal of Geophysical Research: Space Physics, 123, 7609–7620. https://doi.org/10.1029/2018JA025716

Chisham, G. and M. P. Freeman (2003), A technique for accurately determining the cusp-region polar cap boundary using SuperDARN HF radar measurements, *Ann. Geophys.*, 21, 983–996

Chisham, G., M. P. Freeman, and T. Sotirelis (2004), A statistical comparison of SuperDARN spectral width boundaries and DMSP particle precipitation boundaries in the nightside ionosphere, *Geophys. Res. Lett.*, 31, L02804, doi:10.1029/2003GL019074.

Codrescu, M. V., T. J. Fuller-Rowell, and J. C. Foster (1995), On the importance of E-field variability for Joule heating in the high-latitude thermosphere, Geophys. Res. Lett., 22(17), 2393 – 2396.

Cousins, E. D. P., and S. G. Shepherd (2010), A dynamical model of high- latitude convection derived from SuperDARN plasma drift measurements, J. Geophys. Res., 115, A12329, doi:10.1029/2010JA016017.

Cousins, E. D. P., and S. G. Shepherd (2012), Statistical characteristics of small-scale spatial and temporal electric field variability in the high-latitude ionospheres, J. Geophys. Res., 117, A03317, doi:10.1029/2011JA017383.

Cousins, E. D. P., T. Matsuo, and A. D. Richmond (2013), SuperDARN assimilative mapping, *J. Geophys. Res. Space Physics*, 118, 7954-7962, doi:10.1002/2013JA019321.

Cramer, W. D., N. E. Turner, M.-C. Fok, and N. Y. Buzulukova (2013), Effects of different geomagnetic storm drivers on the ring current: CRCM results, J. Geophys. Res. Space Physics,118, 1062–1073, doi:10.1002/jgra.50138.

Davis, T. N., Negative correlation between polar-cap visual aurora and magnetic activity, *J. Geophys. Res.*, 68, 4447, 1963

Deng, Y., and A. J. Ridley (2007), Possible reasons for underestimating Joule heating in global models: E field variability, spatial resolution, and vertical velocity, J. Geophys. Res., 112, A09308, doi:10.1029/2006JA012006.

Denton, M. H., J. E. Borovsky, R. M. Skoug, M. F. Thomsen, B. Lavraud, M. G. Henderson, R. L. McPherron, J. C. Zhang, and M. W. Liemohn (2006), Geomagnetic storms driven by ICME- and CIR-dominated solar wind, J. Geophys. Res., 111, A07S07, doi:10.1029/2005JA011436.

Fuller-Rowell, T. J., et al. (1996), A coupled thermosphere ionosphere model (CTIM), in: STEP
433 Report, R. W. Schunk ed., Scientific Committee on Solar Terrestrial Physics, NOAA/NGDC, 434 Boulder, CO, 239.

Gabrielse, C., Nishimura, Y., Lyons, L., Gallardo- Lacourt, B., Deng, Y., & Donovan, E. (2018). Statistical properties of mesoscale plasma flows in the nightside high- latitude ionosphere. Journal of Geophysical Research: Space Physics, 123, 6798–6820. https://doi.org/10.1029/2018JA025440

Gallardo- Lacourt, B., Y. Nishimura, L. R. Lyons, S. Zou, V. Angelopoulos, E. Donovan, K. A. McWilliams, J. M. Ruohoniemi, and N. Nishitani (2014), Coordinated SuperDARN THEMIS ASI observations of mesoscale flow bursts associated with auroral streamers, J. Geophys. Res. Space Physics, 119, 142–150, doi: 10.1002/2013JA019245.

Gonzalez, W.D., B.T. Tsurutani, A.L.C. Gonzalez, E.J. Smith, F. Tang and S.-I. Akasofu, Solar wind-magnetosphere coupling during intense magnetic storms (1978-1979), J. Geophys. Res., 9, 8835, 1989.

Gonzalez, W. D., Joselyn, J. A., Kamide, Y., Kroehl, H. W., Rostoker, G., Tsurutani, B. T., & Vasyliunas, V. M. (1994). What is a geomagnetic storm? *Journal of Geophysical Research*, *99*(A4), 5771–5792. https://doi.org/10.1029/93JA02867

Gonzalez, W. D., B. T. Tsurutani, and A. L. Clua de Gonzales (1999), Interplanetary origin of geomagnetic storms, Space Sci. Rev., 88, 529

Greenwald, R. A., et al. (1995), DARN/SuperDARN: A global view of high latitude convection, *Space Sci. Rev.*, 71, 763–796.

Guo, J.-P., Deng, Y., Zhang, D.-H., Lu, Y., Sheng, C., & Zhang, S.-R. (2018). The effect of subauroral polarization streams on ionosphere and thermosphere during the 2015 St. Patrick's Day storm: Global ionosphere-thermosphere model simulations. Journal of Geophysical Research: Space Physics, 123, 2241–2256. https://doi.org/10.1002/2017JA024781

Haaland, S. E., G. Paschmann, M. Forster, J. M. Quinn, R. B. Torbert, C. E. McIlwain, H. Vaith, P. A. Puhl-Quinn, and C. A. Kletzing (2007), High-latitude plasma convection from Cluster EDI measurements: method and IMF-dependence, *Ann. Geophys.*, 25, 239–253

Hosokawa, K., J. I. Moen, K. Shiokawa, and Y. Otsuka (2011), Motion of polar cap arcs, J. Geophys. Res., 116, A01305, doi:10.1029/2010JA015906.

Ismail, S., D. D. Wallis, and L. L. Cogger (1977), Characteristics of polar cap Sun-aligned arcs, *J. Geophys. Res.*, 82, 4741.

Johnson, E. S., and R. A. Heelis (2005), Characteristics of ion velocity structure at high latitudes during steady southward interplanetary magnetic field conditions, J. Geophys. Res., 110, A12301, doi:10.1029/2005JA011130.

Knipp, D.,L. Kilcommons, L. Hunt, M. Mlynczak, V. Pilipenko, B. Bowman,Y. Deng, and K. Drake (2013), Thermospheric damping response to sheath-enhanced geospace storms, *Geophys. Res. Lett.*,40,1263–1267, doi:10.1002/grl.50197

Kivanç, Ö., and R. A. Heelis (1998), Spatial distribution of ionospheric plasma and field structures in the high-latitude F region, J. Geophys. Res., 103(A4), 6955–6968, doi:10.1029/97JA03237.

Lassen, K., and C. Danielsen, Quiet time pattern of auroral arcs for different directions of the interplanetary magnetic field in the Y-Z plane, J. Geophys. Res., 83, 5277, 1978

Matsuo, T., A. D. Richmond, and K. Hensel, High-latitude ionospheric electric field variability and electric potential derived from DE-2 plasma drift measurements: Dependence on IMF and dipole tilt., J. Geophys. Res.,108(A1), 1005, doi:10.1029/2002JA009429, 2003.

McGranaghan, R. M., Mannucci, A. J.,& Forsyth, C. (2017). A comprehensive analysis of multiscale field-aligned currents: Characteristics, controlling parameters, and relation-ships. *Journal of Geophysical Research: Space Physics*,122, 11,931–11,960.

Mende, S. B., S. E. Harris, H. U. Frey, V. Angelopoulos, C. T. Russell, E. Donovan, B. Jackel, M. Greffen, M. Peticolas (2008), The THEMIS array of ground-based observatories for the study of auroral substorms, Space Sci. Rev., 141, 357, doi:10.1007/s11212-008-9380-x.

Moen, J., Y. Rinne, H. C. Carlson, K. Oksavik, R. Fujii, and H. Opgenoorth (2008), On the relationship between thin Birkeland current arcs and reversed flow channels in the winter cusp/cleft ionosphere, *J. Geophys. Res.*, 113, A09220,doi:10.1029/2008JA013061.

Moya, P. S., Pinto, V. A., Sibeck, D. G., Kanekal, S. G., & Baker, D. N. (2017). On the effect of geomagnetic storms on relativistic electrons in the outer radiation belt: Van Allen Probes observations. *Journal of Geophysical Research: Space Physics*, 122, 11,100–11,108. https://doi.org/10.1002/2017JA024735

Mursula, K., & Zieger, B. (1996). The 13.5-day periodicity in the Sun, solar wind, and geomagnetic activity: The last three solar cycles. Journal of Geophysical Research, 101(A12), 27,077–27,090. https://doi.org/10.1029/96JA02470

Oksavik, K., J. I. Moen, E. H. Rekaa, H. C. Carlson, and M. Lester (2011), Reversed flow events in the cusp ionosphere detected by SuperDARN HF radars, *J. Geophys. Res.*, 116, A12303, doi:10.1029/2011JA016788.

Pitkänen, T., A. T. Aikio, O. Amm, K. Kauristie, H. Nilsson, and K. U. Kaila (2011), Eiscat-Cluster observations of quiet-time near-Earth magnetotail fast flows and their signatures in the ionosphere, Ann. Geophys., 29(2), 299–319, doi:10.5194/angeo-29-299-2011.

Reimer, A. S., Hussey, G. C., & McWilliams, K. A. (2018). Statistically self-consistent and accurate errors for SuperDARN data. Radio Science, 53, 93–111. https://doi.org/10.1002/2017RS006450

Richardson, I. G., E. W. Cliver, and H. V. Cane (2001), Sources of geomagnetic storms for solar minimum and maximum conditions during 1972–2000, Geophys. Res. Lett., 28, 2569.

Richardson, I.G. and H.V. Cane (2010), Near-Earth Interplanetary Coronal Mass Ejections During Solar Cycle 23 (1996 – 2009): Catalog and Summary of Properties, Solar Phys, 264:189–237, DOI:10.1007/s11207-010-9568-6.

Ridley, A. J., G. Lu, C. R. Clauer, and V. O. Papitashvili (1998), A statistical study of the ionospheric convection response to changing interplanetary magnetic field conditions using the assimilative mapping of ionospheric electrodynamics technique, J. Geophys. Res., 103(A3), 4023–4039, doi:10.1029/97JA03328.

Ridley, A. J., G. Crowley, and C. Freitas, A statistical model of the ionospheric electric potential,
Geophys. Res. Lett., 27, 3675, 2000.

Ridley, A. J., Y. Deng, and G. T´oth, The global ionosphere thermosphere model, Journal of Atmospheric and Solar-Terrestrial Physics, 68, 839–864, doi:10.1016/j.jastp.2006.01.008, 2006.

Rinne, Y., J. Moen, K. Oksavik, and H. C. Carlson (2007), Reversed flow events in the winter cusp ionosphere observed by the European Incoherent Scatter (EISCAT) Svalbard radar, *J. Geophys. Res.*, 112, A10313, doi:10.1029/2007JA012366.

Roble, R. G., and E. C. Ridley (1994), A thermosphere-ionosphere-mesosphere-electrodynamics general circulation model (TIME-GCM): equinox solar cycle minimum simulations (30-500 km), *Geophys. Res. Lett.*, **21**, 417-420.

Shen, X.-C., M. K. Hudson, A. Jaynes, Q. Shi, A. Tian, S. Claudepierre,M.-R.Qin,Q.-G.Zong, and W.-J.Sun (2017), Statistical study of the stormtime radiation belt evolution during Van Allen Probes era: CME- versus CIR-driven storms, J. Geophys. Res. Space Physics,122, 8327–8339,doi:10.1002/2017JA024100.

Sotirelis, T., J. M. Ruohoniemi, R. J. Barnes, P. T. Newell, R. A. Greenwald, J. P. Skura, and C.-I. Meng (2005), Comparison of SuperDARN radar boundaries with DMSP particle precipitation boundaries, *J. Geophys. Res.*, 110, A06302, doi:10.1029/2004JA010732.

Storz, M. F., B. R. Bowman, M. J. I. Branson, S. J. Casali, W. K. Tobiska (2005), High accuracy satellite drag model (HASDM), Adv. Space Res., 36, 2497–2505

Syrjäsuo, M. T. (2001), FMI All-Sky Camera Network Geophysical Publications, Finnish Meteorological Institute, ISBN: 951-697-543-7, ISSN: 0782-6087, 34 pages

Webb, D. F. (1991), The solar cycle variation of the rates of CMEs and related activity, Adv. Space Res., 11, 37.

Weimer, D. R., A flexible, IMF dependent model of high-latitude electric potential having "space weather" applications, Geophys. Res. Lett., 23, 2549, 1996.

Yashiro, S., N. Gopalswamy, G. Michalek, O. C. St. Cyr, S. P. Plunkett, N. B. Rich, and R. A. Howard (2004), A catalog of white light coronal mass ejections observed by the SOHO spacecraft, J. Geophys. Res., 109, A07105, doi:10.1029/2003JA010282.
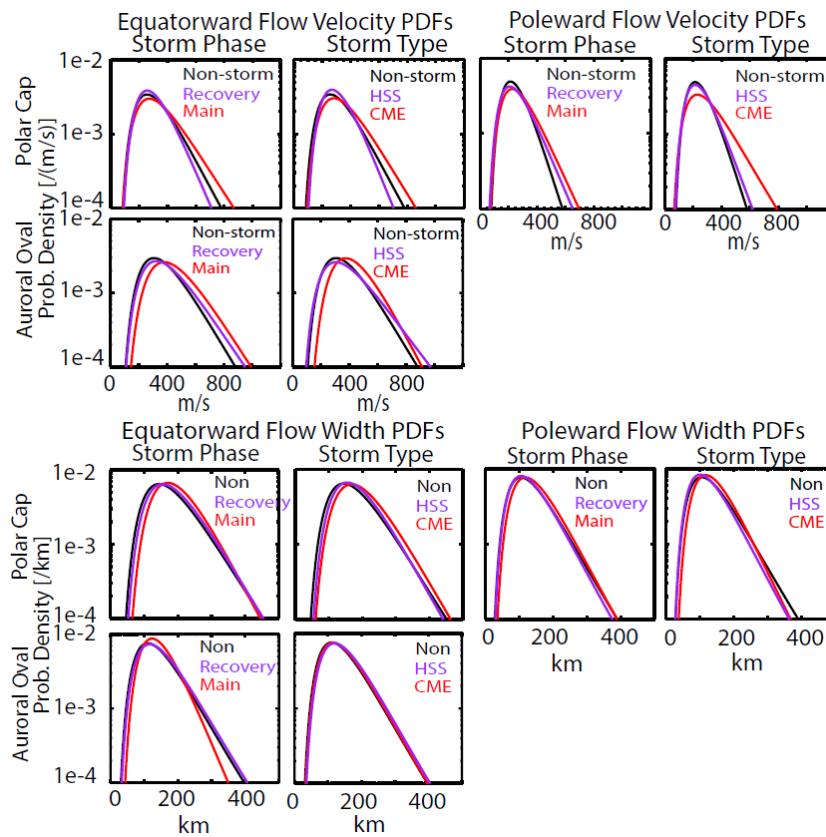
Figure 1. Top six panels: Probability distribution functions of equatorward and poleward flow velocities binned by storm phase and storm type. Bottom six panels: Probability distribution functions of equatorward and poleward flow widths binned by storm phase and storm type.
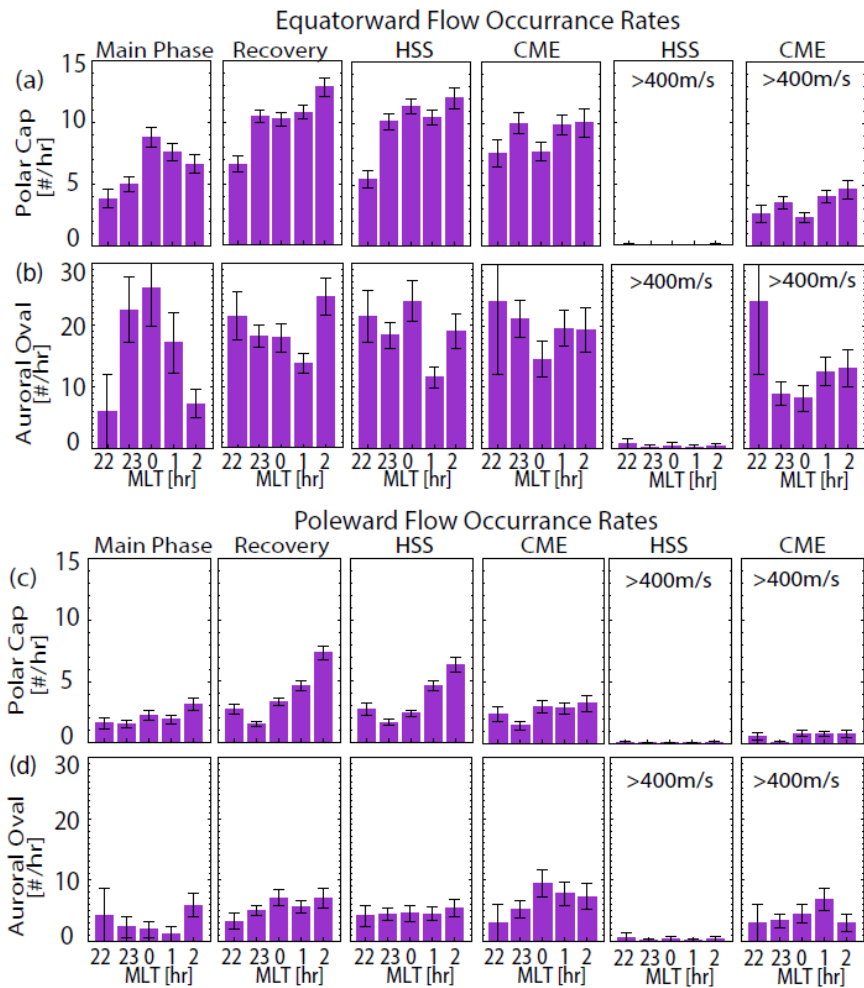
Figure 2. Equatorward flow occurrence rates per MLT bin in the (a) polar cap and (b) auroral oval. Poleward flow occurrence rates per MLT bin in the (c) polar cap and (d) auroral oval. The occurrence rate is the number of SuperDARN scans that observed a meso-scale flow structure normalized by the number of scans that could have observed a flow in that bin.

Table 1. Log-normal Parameters, Medians and Standard Deviations

	Equatorward Width					Equatorward Velocity					
			Median					Median			# of
	μ	σ	[km]	σ		μ	σ	[km]	σ		scans
Non-storm time Polar Cap	2.23	0.17	177	65		2.48	0.18	295	154		48180
Main Phase	2.28	0.14	198	61		2.52	0.19	328	161		447
Recovery Phase	2.25	0.16	192	63		2.47	0.16	293	127		1573
CME	2.28	0.15	204	62		2.53	0.19	337	159		513
HSS	2.25	0.16	186	62		2.48	0.15	300	122		1148
Non-storm time Auroral Oval	2.13	0.19	139	59		2.56	0.18	363	165		5856
Main Phase	2.14	0.15	149	46		2.64	0.16	436	217		59
Recovery Phase	2.15	0.19	146	63		2.59	0.18	388	187		346
CME	2.14	0.18	149	59		2.63	0.15	435	169		157
HSS	2.15	0.18	149	63		2.57	0.20	361	208		233

	Poleward Width					Poleward Velocity					
			Median					Median			# of
	μ	σ	[km]	σ		μ	σ	[km]	σ		scans
Non-storm time Polar Cap	2.11	0.19	136	58		2.39	0.16	239	102		23387
Main Phase	2.14	0.18	151	54		2.43	0.18	273	129		149
Recovery Phase	2.11	0.19	137	56		2.40	0.18	233	122		577
CME	2.14	0.17	144	55		2.45	0.20	282	152		144
HSS	2.09	0.19	127	54		2.39	0.17	233	111		403

Table 2. Kolmogorov-Smirnov Two Sample Test

Equatorward Flow Width		Equatorward Flow Velocity	
Polar Cap	**Distributions**	**Polar Cap**	**Distributions**
CME vs HSS	Unique	CME vs HSS	Unique
CME vs Non	Unique	CME vs Non	Unique
HSS vs Non	Unique	HSS vs Non	Unique
Main vs Recovery	Unique	Main vs Recovery	Unique
Main vs Non	Unique	Main vs Non	Unique
Recovery vs Non	Unique	Recovery vs Non	Unique
Auroral Oval	**Distributions**	**Auroral Oval**	**Distributions**
CME vs HSS	Indistinct	CME vs HSS	Unique
CME vs Non	Indistinct	CME vs Non	Unique
HSS vs Non	*Indistinct*	HSS vs Non	*Indistinct*
Main vs Recovery	Indistinct	Main vs Recovery	Unique
Main vs Non	Indistinct	Main vs Non	Unique
Recovery vs Non	Indistinct	Recovery vs Non	Unique
Poleward Flow Width		**Poleward Flow Velocity**	
Polar Cap	**Distributions**	**Polar Cap**	**Distributions**
CME vs HSS	Unique	CME vs HSS	Unique
CME vs Non	*Indistinct*	CME vs Non	Unique
HSS vs Non	Unique	HSS vs Non	*Indistinct*
Main vs Recovery	Unique	Main vs Recovery	Indistinct
Main vs Non	Unique	Main vs Non	*Indistinct*
Recovery vs Non	Indistinct	Recovery vs Non	Unique